Excitonic Mott insulator in a Bose-Fermi-Hubbard system of moiré WS$_2$/WSe$_2$ heterobilayer

Beini Gao,[1, *] Daniel G. Suárez-Forero*,[1, †] Supratik Sarkar,[1, *] Tsung-Sheng Huang,[1] Deric Session,[1] Mahmoud Jalali Mehrabad,[1] Ruihao Ni,[2] Ming Xie,[3] Jonathan Vannucci,[1] Sunil Mittal,[1] Kenji Watanabe,[4] Takashi Taniguchi,[4] Atac Imamoglu,[5] You Zhou,[2, 6] and Mohammad Hafezi[1, 7, ‡]

[1]*Joint Quantum Institute (JQI), University of Maryland, College Park, MD 20742, USA*
[2]*Department of Materials Science and Engineering,*
University of Maryland, College Park, MD 20742, USA
[3]*Condensed Matter Theory Center, University of Maryland, College Park, MD 20742, USA*
[4]*National Institute for Materials Science, Tsukuba, Japan*
[5]*Institute of Quantum Electronics, ETH Zurich, CH-8093 Zurich, Switzerland*
[6]*Maryland Quantum Materials Center, College Park, Maryland 20742, USA*
[7]*Institute for Theoretical Physics, ETH Zurich, 8093 Zurich, Switzerland*

Understanding the Hubbard model is crucial for investigating various quantum many-body states and its fermionic and bosonic versions have been largely realized separately. Recently, transition metal dichalcogenides heterobilayers have emerged as a promising platform for simulating the rich physics of the Hubbard model. In this work, we explore the interplay between fermionic and bosonic populations, using a WS$_2$/WSe$_2$ heterobilayer device that hosts this hybrid particle density. We independently tune the fermionic and bosonic populations by electronic doping and optical injection of electron-hole pairs, respectively. This enables us to form strongly interacting excitons that are manifested in a large energy gap in the photoluminescence spectrum. The incompressibility of excitons is further corroborated by measuring exciton diffusion, which remains constant upon increasing pumping intensity, as opposed to the expected behavior of a weakly interacting gas of bosons, suggesting the formation of a bosonic Mott insulator. We explain our observations using a two-band model including phase space filling. Our system provides a controllable approach to the exploration of quantum many-body effects in the generalized Bose-Fermi-Hubbard model.

Introduction

The rich physics of the Hubbard model has brought fundamental insights to the study of many-body quantum physics [1]. Initially proposed for electrons on a lattice, different fermionic and bosonic versions of this model have been simulated in various platforms, ranging from ultracold atoms [2] to superconducting circuits [3]. Recently, bilayer transition metal dichalcogenides (TMDs) have become a versatile platform to study the Hubbard model thanks to the coexistence of several intriguing features such as the reduction of electron hopping due to the formation of moiré lattice with large lattice constant, and the existence of both intra- and inter-layer excitons. These characteristics have enabled the realization of numerous effects of many-body physics such as metal-to-Mott insulator transition [4–9], generalized Wigner crystals [10–14], exciton-polaritons with moiré-induced nonlinearity [15], stripe phases [16], light-induced ferromagnetism [17]. Moreover, there have been recent exciting perspectives of exploring such effects in light-matter correlated systems[3, 18, 19].

While typically the fermionic and bosonic versions of the Hubbard model are explored independently, combining these two models in a single system holds intriguing possibilities for studying mixed bosonic-fermionic correlated states. In this work, we demonstrate Bose-Fermi-Hubbard physics in a TMD heterobilayer. We independently control the population of fermionic (electronic) particles by doping with a gate voltage ($V_{\rm g}$), and the population of bosonic (excitonic) states by
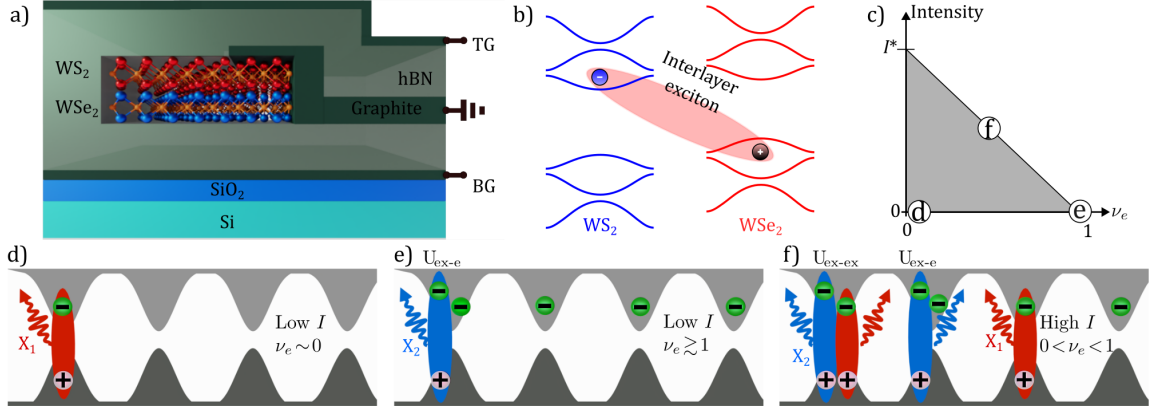
FIG. 1. (a) Schematic of the WS_2/WSe_2 dual-gate device. The TMD heterobilayer is embedded between two symmetric gates: top gate (TG) and bottom gate (BG). (b) Depiction of the type-II band alignment of the bilayer. The blue and red curves denote bands from WS_2 and WSe_2, respectively. The shaded ellipse indicates the formation of interlayer excitons composed of an electron from the WS_2 conduction band and a hole from the WSe_2 valence band. (c) Phase diagram of the system. The population of the moiré lattice can be controlled via two independent parameters: the gate voltage changes the electronic filling factor (ν_e), and the optical pump creates a population of excitons, proportional to the input intensity. In the gray area, the system behaves as a mixed gas of bosonic and fermionic particles. As one approaches the upper limit (black line), the system becomes incompressible due to the saturation of single occupancy states. (d-f) Interlayer exciton formation under optical excitation for three different regimes governed by the pump intensity (I) and ν_e: (c) low I and $\nu_e \sim 0$, (d) low I and $\nu_e \sim 1$, (e) high I and $0 < \nu_e < 1$. X_1 (X_2) denotes PL emission from singly (doubly) occupied moiré lattice sites. X_2 can originate from either electron-exciton (U_{ex-e}) or exciton-exciton (U_{ex-ex}) double occupancies.

pumping with a pulsed optical drive of intensity I. Harnessing these two control methods, we realize strongly interacting excitons. In particular, we show the incompressibility of excitonic states near integer filling by observing an energy gap in photoluminescence, accompanied by an intensity saturation. More remarkably, we observe the suppression of diffusion, as a strong indication of the formation of bosonic Mott insulator of excitons.

To demonstrate these effects, we use a moiré lattice created by stacking two monolayers of WS_2 and WSe_2, with symmetric top and bottom gates. Fig. 1a shows a schematic illustration of the heterobilayer device (details in the Supplementary Material). The type-II band alignment of the heterostructure results in the formation of an energetically favorable inter-layer exciton (X) [20], by pairing an electron in WS_2 with a hole in WSe_2 (Fig. 1b). In order to explore different regimes of Bose-Fermi-Hubbard model, we control the bosonic and fermionic populations by changing I and V_g, respectively. This can be compared to ultra-cold atom implementation of Bose-Fermi mixture where the respective populations are fixed in each experiment [21]. Before discussing our experimental observation, we discuss three limiting cases that determine the phase space of our system, as indicated in Fig. 1c. The corresponding physical scenarios are represented in panels d to f. First, in the weak excitation limit and low electronic filling factor ($\nu_e \sim 0$) regime, the system's photoluminescence (PL) emission originates exclusively from the few X states in the quasi-empty lattice (panel d). This emission comes from excitons in lattice sites where they are the only occupant particles, namely, "single occupancy states" (X_1). Upon increasing ν_e, the number of singly occupied

sites increases, and in the limiting case of $\nu_e \geq 1$, as represented in panel e, the optically generated excitons can only form in lattice sites already occupied by charged particles. In this case, the required energy to form the exciton increases due to the on-site Coulomb repulsion, and hence the PL emission has new branch with higher energy than the previous regime. Consequently, the PL originates from lattice sites with an electron-exciton double occupancy (X_2). Finally, we consider the case where the electrical doping is below the threshold required to reach a fermionic Mott insulator ($0 < \nu_e < 1$) but I is strong enough to optically saturate the single occupancy states. The extra excitons create a number of sites with electron-exciton or exciton-exciton double occupancies (panel f). We later discuss that, within our experimental resolution, these latter two situations are not spectrally resolvable. Therefore, in this regime, the emitted light is only a combination of the X_1 and X_2 PL emission. This interplay between exciton and electron occupancy can lead to situations in which the moiré lattice is completely filled with a mixed population of fermions and bosons, forming a hybrid incompressible state. Specifically, in the limit of weak electronic tunneling, excitons can form a Mott insulating state, in the remainder of sites that are not filled by electronic doping. Note the line in Fig. 1c denoting panel f is an asymptote, since optical pumping can not fully saturate an exciton line. At $\nu_e = 0$, this intensity is denoted as I^*. (details in the Supplementary Material).

Results

To experimentally investigate these regimes, we perform PL measurements, with varying pump power and backgate voltage. A detailed description of the optical setup can be found in the Supplementary Material. Fig. 2a-c shows the PL dependence at three different intensities as schematically shown in panel d. Fig. 2a shows the normalized doping-dependent PL spectrum for low I ($0.08 \mu W/\mu m^2$), which corresponds to low bosonic occupation. The fermionic occupation ν_e is varied between 0 and 1.1. For low ν_e, PL emission is detected only from X_1. However, at $V_g \approx 2.98$V, we detect a transition in the PL emission to X_2. This transition corresponds to the formation of X's in presence of an incompressible fermionic Mott insulator [22, 23]. From the reflectivity measurement and calculations from a capacitor model, we attribute $V_g = 2.98$ V to $\nu_e = 1$ (see Supplementary Material). The energy gap between X_1 and X_2 is $\Delta E \approx 29$meV, which corresponds to the on-site Coulomb repulsion energy between an electron and an exciton. We elaborate on this energy gap later in the discussion of Fig. 5. The dim features between X_1 and X_2 at $\nu_e \sim 1$ are likely caused by mid-gap states generated by localized excitons. Fig. 2b shows the PL spectrum under pump intensity equal to 12.1 $\mu W/\mu m^2$. It is worth noticing that the V_g at which the PL signal from X_2 is detected, is lower than in panel a. The system is therefore in the regime depicted in Fig. 1f. Upon further increasing the pump intensity X_2 can be detected even at $\nu_e = 0$, as observed in Fig. 2c. In this case, the PL emission originates solely from double occupancy of excitons in a moiré lattice site, suggesting that, for high I, purely bosonic states of strongly interacting excitons are created.

From the observation described in the previous paragraph, we conclude that the detection of PL emission with X_1 and X_2 energies benchmarks the formation of exciton states in singly and doubly occupied lattice sites, respectively. Next, in order to understand the interplay between fermionic and bosonic lattice occupancies in each regime, we perform a quantitative analysis of their respective integrated intensity. We extract these values from the collected PL spectra using a computational fitting method (see Supplementary Material for further details). Fig. 2e-g displays this intensity dependence on ν_e for the same I range of panels a-c. We notice that as electrons gradually fill
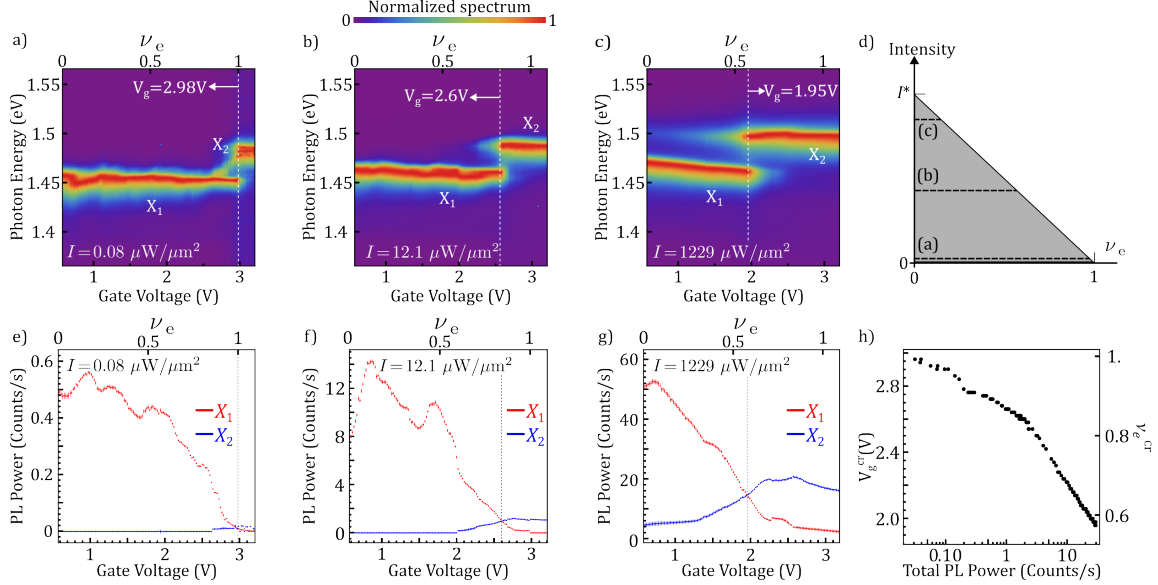
FIG. 2. (a-c) Evolution of the PL spectrum as a function of gate voltage (ν_e) for three different pump intensities: I = $0.08\mu W\mu m^2$ (a), I = $12.1\mu W/\mu m^2$ (b) and I = 1229 $\mu W/\mu m^2$ (c). The peaks associated with single (X_1) and double (X_2 occupancy are indicated on each panel. The dashed lines indicate the gate voltages at which the PL intensity X_2 exceeds X_1. The dashed black lines of panel (d) indicate the measurement ranges of (a-c). (e-f) Evolution of the PL intensity for X_1 (red) and X_2 (blue) as a function of gate voltage for the same values of pump intensities displayed in panels (a-c). The electron filling factor at which X_2 exceeds X_1 decreases as pump intensity increases. Panel (h) shows the gate voltage at which the intensity of X_2 exceeds that of X_1, as a function of the total PL intensity.

the system (upon increasing V_g), the number of accessible single-occupancy states decreases. As a consequence, the integrated intensity of X_1 reduces with increasing ν_e. Remarkably, for each intensity, there is a critical ν_e after which the PL emission of X_2 exceeds that of X_1. The gate voltage at which the crossing takes place (V_g^{cr}) is highlighted on each panel by a vertical dashed line. This line indicates the scenario where the number of doubly occupied sites becomes higher than the number of singly occupied sites, assuming that the radiative decay rate of both lines is similar. The crossing takes place at lower ν_e upon increasing I, as expected. In Fig. 2h, we track V_g^{cr} as a function of the total collected PL emission, which we assume is proportional to the total number of excitons in both X_1 and X_2 branches. We choose this quantity, rather than the input pump intensity because the latter is not proportional to the total number of created excitons (see Supplementary Material for further details). We observe a clear trend: a higher total population of excitons results in a faster saturation of the single occupancy states and hence an increasing number of double occupancy states.

Next, in order to trace the role of the optical pump and the optical saturation that leads to the formation of incompressible bosonic states, we investigate the PL for varying I for different ν_e. In Fig. 3a-c, we focus on three different values of ν_e, as indicated in panel d, and study the PL spectrum for increasing emitted PL power. For zero fermionic occupancy (panel a), X_2 contributes to the emission only at very high total PL emission intensity. In panels b and c, we increase the electrical
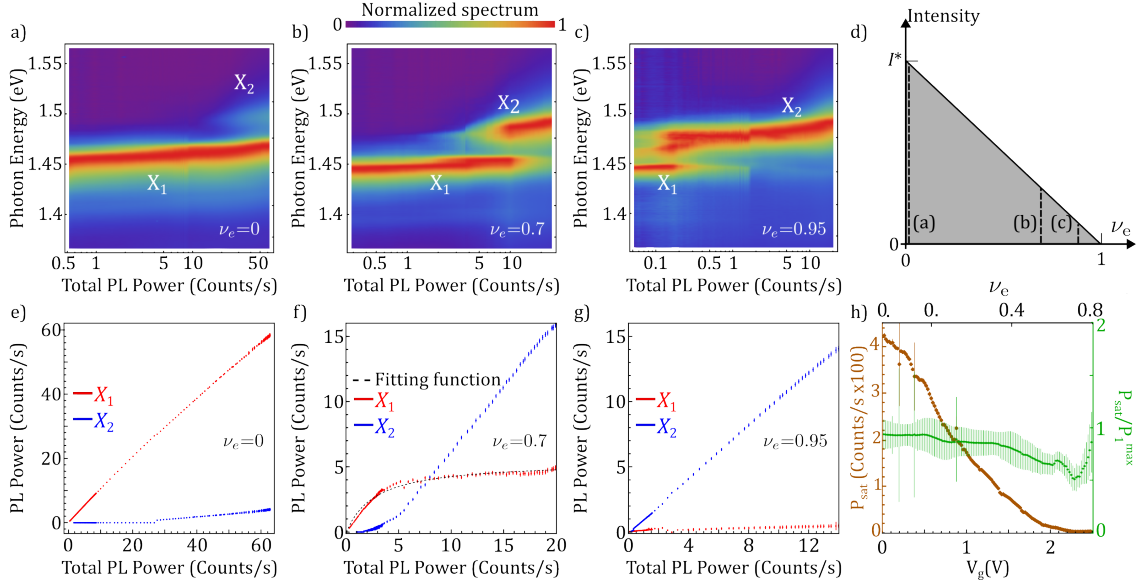
FIG. 3. (a-c) Evolution of the normalized PL spectrum as a function of the total collected PL power for three different electronic filling factors. The peaks associated with single (X_1) and double (X_2) occupancy are indicated on each panel. Panel (d) indicates the ranges of I and ν_e for the measurements shown in panels (a-c). (e-f) evolution of the PL power for X_1 (red) and X_2 (blue) as a function of the total collected PL power for the same values of ν_e displayed in panels (a) to (c). Panel (f) displays the fitting function (dashed black line) employed to extract P_{sat} and P_1^{max} (described in the text). (g) Evolution of P_{sat} (brown) as a function of the gate voltage (ν_e). As expected from our phase-space filling model, its value reduces with increasing filling factor. The quantity P_{sat}/P_1^{max} (green) shows good agreement with the theoretical model.

doping to $\nu_e = 0.7$ and $\nu_e = 0.95$, respectively. The total PL at which we detect X_2 decreases consequently. At low powers, the X_1 line exhibits a blueshift. Assuming negligible tunneling, the shift should be equal to $U_{ex-ex}\langle a^\dagger a \rangle$, where $a^\dagger$ is the creation operator of an exciton. For example, in Fig. 3b for total PL power at 2 counts/s, the bosonic occupation is $\langle a^\dagger a \rangle \simeq 0.2$. This corroborates with the energy gap that occurs at 10 counts/s for an estimated $\langle a^\dagger a \rangle \simeq 1$. Panels e-g show the intensities of X_1 and X_2 for the values of ν_e in panels a-c. As expected, in panel e, one can observe that the intensity of the X_1 PL emission increases monotonically, and it starts to saturate only at very high total PL emission regimes. Upon filling the moiré lattice with one exciton or one electron per site, the X_1 PL intensity saturates. With higher ν_e, the saturation occurs at lower I, as shown in panels f and g. Since this saturation corresponds to filling the single occupancy states, we associate this saturation with the establishment of an incompressible bosonic Mott insulator. Note that this bosonic Mott insulator is in a drive-dissipative regime, similar to the demonstration in superconducting qubit systems [24].

To quantitatively analyze this saturation effect, we fit the X_1 PL power (P_1) to the function $P_1 = P_1^{max}\frac{P}{P+P_{sat}}$, where P is the total PL power. From the fitting, we extract P_1^{max} which is the asymptotic value of the X_1 emitted PL power, and P_{sat} which determines the total PL of saturation. This functional form corresponds to the expected behavior of the system when the
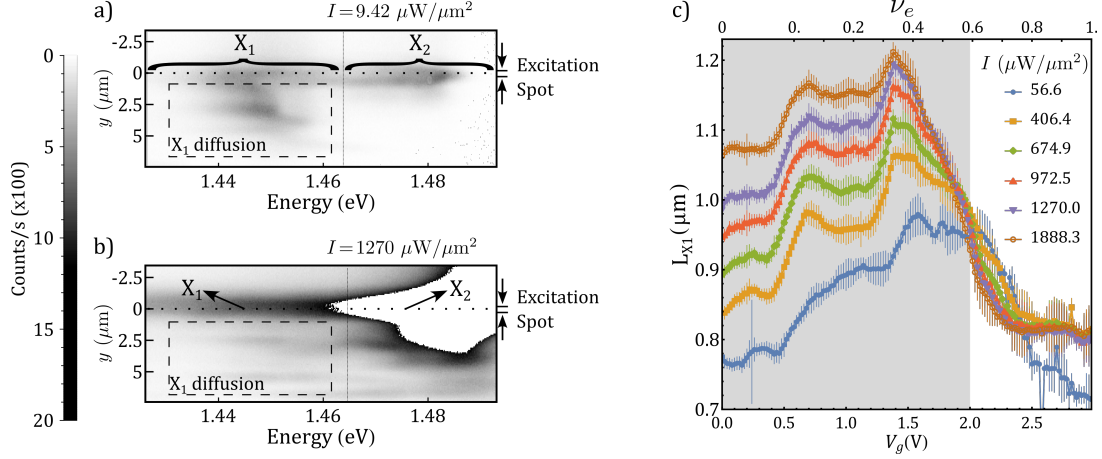
FIG. 4. Spectrally and spatially-resolved diffusion pattern at $\nu_e = 0.73$ ($V_g = 2.34$V) for low (a) and high (b) I. The dashed rectangle highlights the region where the suppression of diffusion can be observed. (c) Exciton diffusion length as a function of the gate voltage for a range of ν_e and for different input intensities. For low ν_e (highlighted in grey) the diffusion length increases with I due to exciton repulsive interaction. Upon further filling the moiré lattice (dashed line), the trend changes around $\nu_e \simeq 0.6$, indicating the optical realization of incompressible states.

charge gap U is large enough to allow the use of a phase-space filling model treatment of the single and double occupancy states (details in the Supplementary Material). Fig. 3f includes an example of the fitting function (dashed black line). According to our model, the value of P_{sat} should decrease with increasing ν_e because a lower excitonic population is required to achieve the incompressible states. The compiled data for the full range of ν_e, shown in panel h with brown marks, is in good agreement with the expected trend. From the model, we can also infer that the quantity P_{sat}/P_1^{max} should be independent of the electronic doping level because both quantities depend linearly on $1 - \nu_e$; higher electronic occupancy implies less single occupancy states available to host an exciton. The green marks in Fig. 3h represent this behavior, which is in good agreement with the model. We conclude that the saturation of the single occupancy states directly manifests in the intensity of X_1, which allows extracting the condition at which the incompressible states take place. Importantly, this allows a direct calibration of the bosonic and fermionic fractions in the system.

In order to further validate the incompressible nature of excitonic states, we perform diffusion measurements of the interlayer excitons [25]. For a steady population of excitons, created by a continuous-wave laser pump, the diffusion length carries information about the nature of the state: an incompressible bosonic state is expected to have a lower diffusion length than a weakly interacting one. We spatially image the diffusion pattern with spectral resolution and extract the diffusion length (L_{X1}) of the single occupancy excitons. The optically-induced suppression of the diffusion length for constant ν_e can be clearly observed in Fig. 4a-b. The population injected at $y = 0$ (dotted line) propagates, and its emission pattern is monitored along a range of 5 μm (dashed rectangle). The color scale is the same for both panels. Panel b shows a reduction of the diffused X_1 population in comparison to panel a. Fig. 4c shows the extracted L_{X1} as a function of V_g and for different pump intensities from the exponentially decaying spatial diffusion pattern in the negative y region (details in the Supplementary Material). For $\nu_e \lesssim 0.6$ ($V_g \lesssim 2.0$V), highlighted in
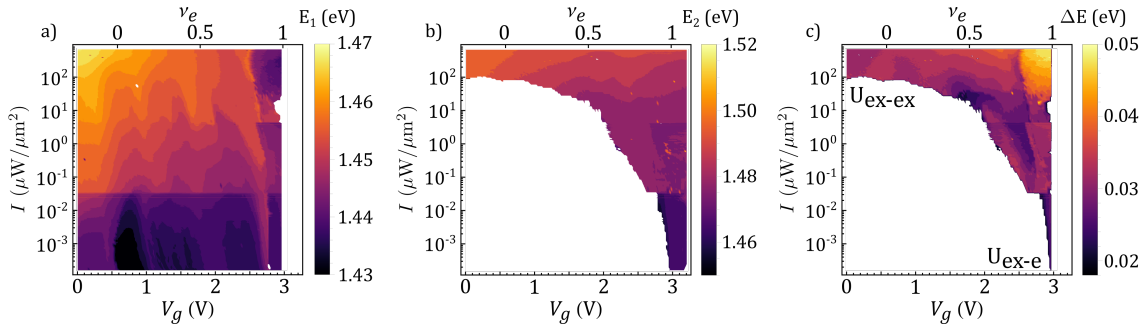
FIG. 5. Energy of the X_1 (a) and X_2 (b) PL emission as a function of gate voltage and pump intensities. The white areas correspond to the range of parameters where the corresponding peak completely vanishes. When X_1 and X_2 coexist, we extract the energy difference, as shown in panel (c).

grey, the trend is in agreement with the expected behavior for weakly interacting bosons [26, 27]. Remarkably, as the electronic filling factor increases, the trend completely changes. In particular, around $\nu_e \lesssim 0.6$, L_{X1} reduces with increasing intensity, and for higher ν_e, the diffusion becomes constant. This is a direct signature of the bosonic Mott insulator formation, since the bulk is incompressible and the melting only occurs at the edge.

Outlook

In summary, we demonstrated a Mott insulating state of excitons in a hybrid Bose-Fermi Hubbard system formed in a TMD heterobilayer. While our incompressibility observation was based on spatially resolved diffusion in the steady-state limit, one can explore interesting non-equilibrium physics due to the relatively long lifetime of interlayer excitons. More generally, spatiotemporally resolved measurements, combined with independent tunability of fermionic and bosonic populations, make it possible to investigate the equilibrium and non-equilibrium physics of Bose-Fermi mixtures. Particularly intriguing examples are the optical investigation of charge and spin physics in integer and fractional fillings, e.g., Mott excitons [28, 29] or spin liquids [30–33], and fractional Chern insulators [34, 35].

During the course of this project, the authors became aware of other works exploring the interaction between interlayer excitons in similar systems [36].

Acknowledgements

Supporting Information

Device fabrication

The WSe$_2$/WS$_2$ heterostructure shown in Fig. S1 was fabricated using a dry-transfer method with a stamp made of a poly(bisphenol A carbonate) (PC) layer on polydimethylsiloxane (PDMS) [37]. All flakes were exfoliated from bulk crystals onto Si/SiO$_2$ (285 nm) and identified by their optical contrast. The top/bottom gates and TMD contact are made of few-layer graphene. The PC stamp and samples were heated to 60°C during the pick-up steps and released from the stamp to the substrate at 180°C. The PC residue on the device was removed in chloroform followed by a rinse in isopropyl alcohol and ozone clean. Sample transfer was performed in an argon-filled glovebox for improved interface quality. The electrodes consist of 3.5 nm of chromium and 70 nm of gold. They were fabricated using standard electron-beam lithography techniques and thermal evaporation.
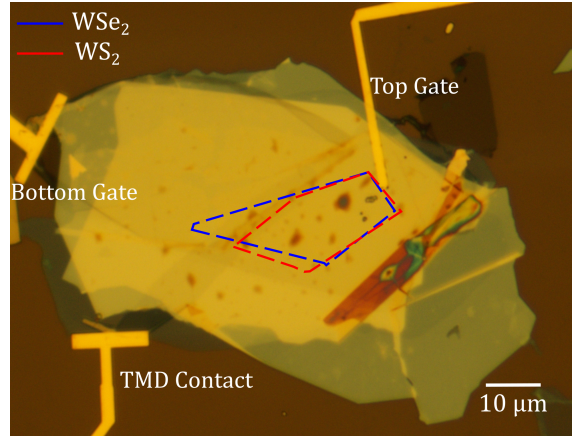

FIG. S1. Microscope image of the WS$_2$/WSe$_2$ heterostructure device.

Optical measurements

The sample is kept in a dilution refrigerator at a temperature of 3.5K. For photoluminescence measurements, we use a confocal microscopy setup with an objective of magnification 70× and numerical aperture NA = 0.82. Our pumping source is a pulsed Ti:Sapphire laser tuned at 720nm (1.722eV), with a pulse duration of 100fs and a repetition rate of ∼ 80 MHz. A half-waveplate placed before a polarizing beam-splitter is rotated to control the pump power. Additionally, an optical chopper system at 800Hz is used to prevent sample heating while having a high pump intensity. A 750nm long-pass filter was used to block the residual pump laser before collecting the PL emission in a spectrometer equipped with a 300 grooves per mm diffraction grating and a CCD camera. The schematic of the setup is shown in Fig. S2.

For the diffusion measurements, we used a continuous-wave (CW) Ti:Sapphire laser tuned at 708nm. The rest of the optical measurement setup was similar. By applying a spatial filter to the reconstructed image of the diffusion pattern, we obtain spectral and spatial data of the exciton emission. This allows to image the spatial diffusion of each spectral component and extract the diffusion length.
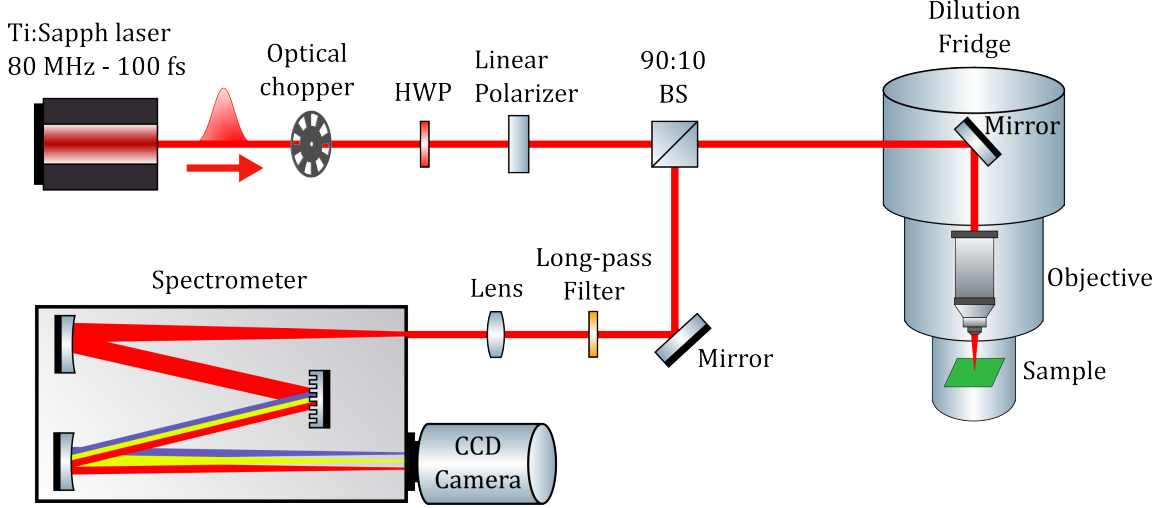

FIG. S2. Schematic of the experimental setup. HWP=Half-wave plate, BS=Beam splitter

Electronic filling factor calibration

The electronic filling factor (ν_e) can be estimated by combining the information about the crystalline structure of the bilayer device and a parallel capacitor model, as follows:

Determination of moiré density n_0: In a purely fermionic Mott insulating state, the heterostructure will host one electron per moiré unit cell. The charge density in this case is given by n_0, and it can be directly determined by the moiré periodicity through the relationship $n_0 = 1/(L_M{}^2 \sin \pi/3)$. Here, $L_M = a/\sqrt{\delta^2 + \theta^2}$ is the size of the moiré superlattice, $\delta = (a-a')/a \approx 4\%$ is the lattice mismatch between WSe_2 ($a = 0.328$nm) and WS_2 ($a' = 0.315$nm), and θ is the twist angle between the two layers. Assuming $0° \leq \theta \leq 1°$, we obtain $1.72 \times 10^{12} \text{cm}^{-2} \leq n_0 \leq 2.04 \times 10^{12} \text{cm}^{-2}$.

Determination of electron density n_e: From a parallel capacitor model, we can deduce the expression for the electron density (n_e) in the bilayer. For a dual gate device, n_e is given by:

$$n_e = \frac{\epsilon_r \epsilon_0 \Delta V_g}{d_t} + \frac{\epsilon_r \epsilon_0 \Delta V_g}{d_b},$$

where V_g is the symmetrically applied gate voltage and $d_t \approx d_b \approx 40$nm are the thicknesses of the top and bottom hBN dielectrics, respectively. They are determined from the optical contrast of the hBN flakes under the microscope. ϵ_0 is the vacuum permittivity, and $\epsilon_r \approx 3$ is the relative permittivity of hBN [38]. Having the moiré density n_0 and the electron density n_e, the electronic

(fermionic) filling factor can be expressed as $\nu_e = n_e/n_0$. From this model we deduce that the gate voltage at which the electronic Mott insulator is established lies in the range 2.65 V$<V_g<$3.04 V. Where we are taking into account that the neutral region extends up to $V_g=0.58$ V. This estimation is in good agreement with our experimental data for reflectivity and PL. The results, displayed in Fig. S3 show a consistent change in the optical response of the device at $V_g = 2.98$ V. For the reflectivity (panel a), we observe a shift in the intralayer exciton energy. For the PL (panel b), a corresponding energy transition is observed for the interlayer exciton.
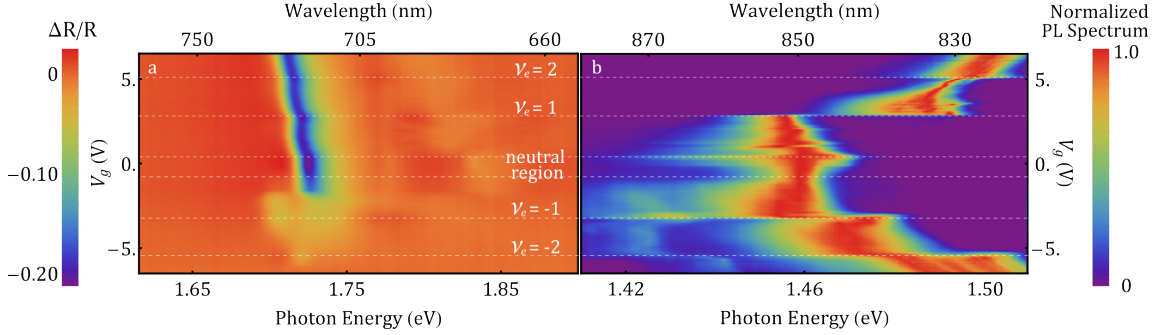

FIG. S3. Reflection and photoluminescence spectra of our WS_2/WSe_2 heterobilayer device.

Total emitted PL vs. Pump Intensity

Due to the saturability of real semiconductor materials upon an intense optical pump, the laser intensity I is not a suitable parameter to estimate the total exciton density in the bilayer. One can corroborate this from Fig. S4, by noticing that the emitted PL power does not follow a linear trend with increasing I. A more suitable quantity to monitor the changes in the excitonic density is the total emitted PL power. This quantity can be considered proportional to the total number of excitons formed in the structure, with the proviso that the radiative decay of the excitons does not change considerably within the phase space determined by V_g and I. For this reason, figures 2 and 3 of the main text display the total PL power instead of the pump intensity. For simplicity, all the PL powers presented in the main text are normalized to a factor 10^6.

Data analysis

To obtain relevant information about the collected spectra, we use a fitting routine. This procedure allows us to obtain the PL emission central energy, linewidth, and integrated PL power of each exciton line (X_1 and X_2). First, the PL spectra are processed by removing background noise and applying a low-pass Butterworth filter. After that, we extract the peaks from each spectrum by imposing constraints on the energy range, linewidth, prominence, and relative amplitude to the noise level. By setting a tolerance to the numerical error of the obtained values of intensity and energy of each peak, we fit each spectrum to a multi-Lorentzian distribution. From the fitting functions,
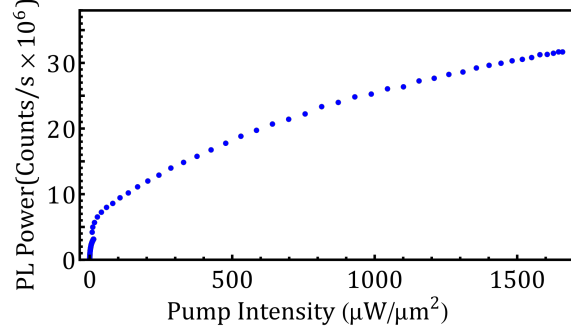
FIG. S4. Pump intensity dependent total PL power at $V_{\mathrm{g}} = 0$V

we extract the central energies of X_1 and X_2 and integrate them over the obtained distributions to get the individual PL power.
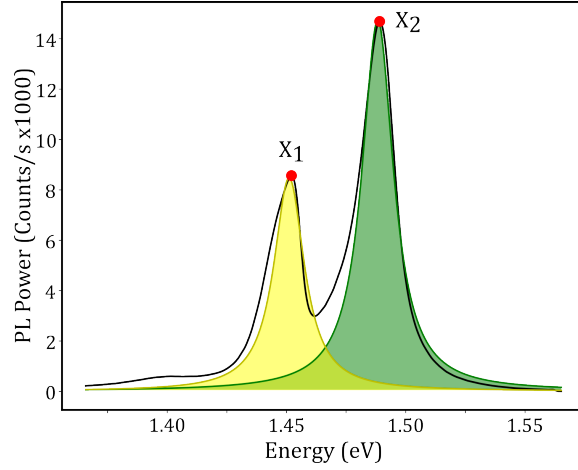

FIG. S5. A typical PL spectrum ($V_{\mathrm{g}} = 2.1$ V and $I = 2226$ $\mu\mathrm{W}/\mu\mathrm{m}^2$) with the fitting functions obtained from the numerical method.

Modeling X_1 and X_2

To obtain further insights into the physical mechanism dominating the system dynamics, we make a theoretical analysis using a 2-band model, as mentioned in the main text. Our goal is to deduce an analytical expression for the observed saturation behavior of the PL power from the X_1 population. This is achieved by considering the steady state of the system in a continuous-wave excitation regime. A population of electron-hole pairs n_{eh} is created by a Rabi-driving $\Omega(t)$. The charged plasma cascades down and relaxes to create n_1 singly occupied moiré sites (X_1) and n_2 doubly occupied sites (X_2). The formation of those states depends on the relaxation rate of the

plasma (Γ_{relax}), the maximum number of available lattice sites ($n_{\max}(\nu_e)$), and a β factor, which determines the probability of the plasma to decay into the X_1 state. Under these conditions, the system's dynamics can be described by the set of equations:

$$\frac{\mathrm{d}n_{\text{eh}}}{\mathrm{d}t} = \eta \left| \Omega(t) \right|^2 - \Gamma_{\text{relax}} n_{\text{eh}} \tag{S1a}$$

$$\frac{\mathrm{d}n_1}{\mathrm{d}t} = \Gamma_{\text{relax}} \beta \frac{n_{\max}(\nu_e) - n_1}{n_{\max}(\nu_e)} n_{\text{eh}} - \Gamma_1 n_1 \tag{S1b}$$

$$\frac{\mathrm{d}n_2}{\mathrm{d}t} = \Gamma_{\text{relax}} \left(1 - \beta \frac{n_{\max}(\nu_e) - n_1}{n_{\max}(\nu_e)} \right) n_{\text{eh}} - \Gamma_2 n_2 \tag{S1c}$$

where η is the efficiency of the optical generation of electron-hole pairs and Γ_1 (Γ_2) is the decay rate of the excitonic states in a singly (doubly) occupied site. In a steady state condition, from Eq. S1b, we can obtain an analytical expression for n_1:

$$n_1 = \frac{\Gamma_{\text{relax}} \beta n_{\text{eh}}}{\Gamma_1 + \Gamma_{\text{relax}} \beta \frac{n_{\text{eh}}}{n_{\max}}} \tag{S2}$$

In this regime n_{eh} reaches an asymptotic value $n_{\text{eh}} = \frac{\eta}{\Gamma_{\text{relax}}} \left| \Omega \right|^2$. To associate this expression with our experimental data, we take into account that $n_{\text{eh}} \Gamma_{\text{relax}}$ is proportional to the total PL power and n_1 is proportional to the PL power (P_1) from the X_1 exciton band. After substituting variables we can conclude that the saturation behavior of X_1 should follow the functional form:

$$P_1 = P_1^{\max} \frac{P}{P + P_{\text{sat}}} \tag{S3}$$

where $P_1^{\max} = n_{\max}$ is proportional to the PL power from X_1 in an ideal Mott insulating state and $P_{\text{sat}} = \Gamma_1 n_{\max} / \beta$ determines the total PL emission at which X_1 saturates. This expression is used as a fitting model for the PL power from the X_1 states upon increasing total PL power, and provides a mathematical tool to estimate the bosonic occupation of the moiré lattice. From this theoretical treatment, one can notice that the bosonic Mott insulating states are reached asymptotically. This means that P_1 can be arbitrarily close to $P_1^{\max}$ upon a high enough total PL power. In other words, the line that determines the Mott insulating phases in Figs. 1c, 2d and 3d is mathematically not achievable. For this reason, the intensity denoted as I^* in the referred figures, indicates the required pump intensity to drive the system into a state with a total population arbitrarily close to the lattice complete saturation.

Theoretical estimate of U_{ex-e} and U_{ex-ex}

For an electron and an exciton occupying the same moiré potential, we can express the interaction energy as

$$U_{ex-e} \sim \frac{e^2}{\epsilon_r} \int d^2 \mathbf{r}_x^{\text{com}} d^2 \mathbf{r}_x^{\text{rel}} d^2 \mathbf{r}_e \left| W \left(\mathbf{r}_x^{\text{com}} \right) \Phi \left(\mathbf{r}_x^{\text{rel}} \right) \right|^2 \left| \Psi \left(\mathbf{r}_e \right) \right|^2 \frac{1}{\left| \mathbf{r}_x + \frac{m_v}{m_x} \mathbf{r}_x^{\text{rel}} - \mathbf{r}_e \right|}, \tag{S4}$$

where e is the charge of electron, ϵ_r is the dielectric constant, $\mathbf{r}_x^{\text{com}}$ is the center-of-mass co-ordinate of the exciton, $\mathbf{r}_x^{\text{rel}}$ is the relative co-ordinate of the exciton, $\mathbf{r}_e$ is the co-ordinate of the electron, $W\left(\mathbf{r}_x^{\text{com}}\right)\Phi\left(\mathbf{r}_x^{\text{rel}}\right)$ is the wavefunction of the exciton in terms of center-of-mass and relative co-ordinates, $\Psi\left(\mathbf{r}_e\right)$ is the electron's wavefunction, m_v is the mass of the hole, and m_x is the mass of the exciton.

The excitonic and electronic wavefunctions can be expressed as

$$W\left(\mathbf{r}_x^{\text{com}}\right) \sim \frac{1}{\sqrt{\pi}}\frac{1}{a_W^x}\exp\left[-\frac{1}{2}\left(\frac{\mathbf{r}_x^{\text{com}}}{a_W^x}\right)^2\right], \tag{S5a}$$

$$\Phi\left(\mathbf{r}_x^{\text{rel}}\right) \sim \sqrt{\frac{\pi}{2}}\frac{a_B}{2}\exp\left[-\frac{2\mathbf{r}_x^{\text{rel}}}{a_B}\right], \tag{S5b}$$

$$\Psi\left(\mathbf{r}_e\right) \sim \frac{1}{\sqrt{\pi}}\frac{1}{a_W^e}\exp\left[-\frac{1}{2}\left(\frac{\mathbf{r}_e}{a_W^e}\right)^2\right], \tag{S5c}$$

where $a_W^{x(e)}$ is the Wannier orbital size of the exciton (electron), and a_B is the Bohr radius of the exciton.

Similarly, the exciton-exciton interaction energy can be expressed as

$$U_{ex-ex} \sim \frac{e^2}{\epsilon_r}\int d^2\mathbf{r}_{x1}^{\text{com}}d^2\mathbf{r}_{x1}^{\text{rel}}d^2\mathbf{r}_{x2}^{\text{com}}d^2\mathbf{r}_{x2}^{\text{rel}}\left|W\left(\mathbf{r}_{x1}^{\text{com}}\right)\Phi\left(\mathbf{r}_{x1}^{\text{rel}}\right)\right|^2\left|W\left(\mathbf{r}_{x2}^{\text{com}}\right)\Phi\left(\mathbf{r}_{x2}^{\text{rel}}\right)\right|^2$$
$$\times\frac{1}{\left|\mathbf{r}_{x_1}^{\text{com}} - \mathbf{r}_{x_2}^{\text{com}} - \alpha\mathbf{r}_{x1}^{\text{rel}} - \beta\mathbf{r}_{x2}^{\text{rel}} + \mathbf{z}\right|}, \tag{S6}$$

where subscripts 1, 2 indicate the two excitons, $\mathbf{z}$ is the interlayer distance, and α, β are coefficients that can take values of $\pm\frac{m_c}{m_x}$ or $\pm\frac{m_v}{m_x}$, where m_c is the mass of an electron.

We use an interlayer distance of $z = 0.6$ nm, exciton Bohr radius $a_B = 2$ nm, relative permittivity $\epsilon_r = 5$, moiré period of $a_M = 10$ nm, and Wannier orbital size of exciton $a_W^x = 2.8$ nm. We also consider $a_W^e \approx \sqrt{2}a_W^x$ for electrons and holes being in the same moiré potential and having similar mass. Using these values, we estimate the interaction energies to be: $U_{ex-ex} \sim 27$ meV and $U_{ex-e} \sim 90$ meV. However, one must note that in the calculation for U_{ex-e} we have neglected the contribution of the interaction between the hole and the electron as it will be partially cancelled by background charge. Thus, strictly speaking, $U_{ex-e} \sim 90$ meV is only an estimated upper bound.

Diffusion measurements

For the diffusion measurements, we use a continuous-wave laser tuned at 708 nm to create a steady population of excitons. By imaging the diffusion pattern with spectral resolution, we are capable of monitoring the diffusion properties of the X_1 and X_2 populations. We study the dependence of the diffusion length for each population as a function of V_{g} and I. To improve the spatial resolution, the
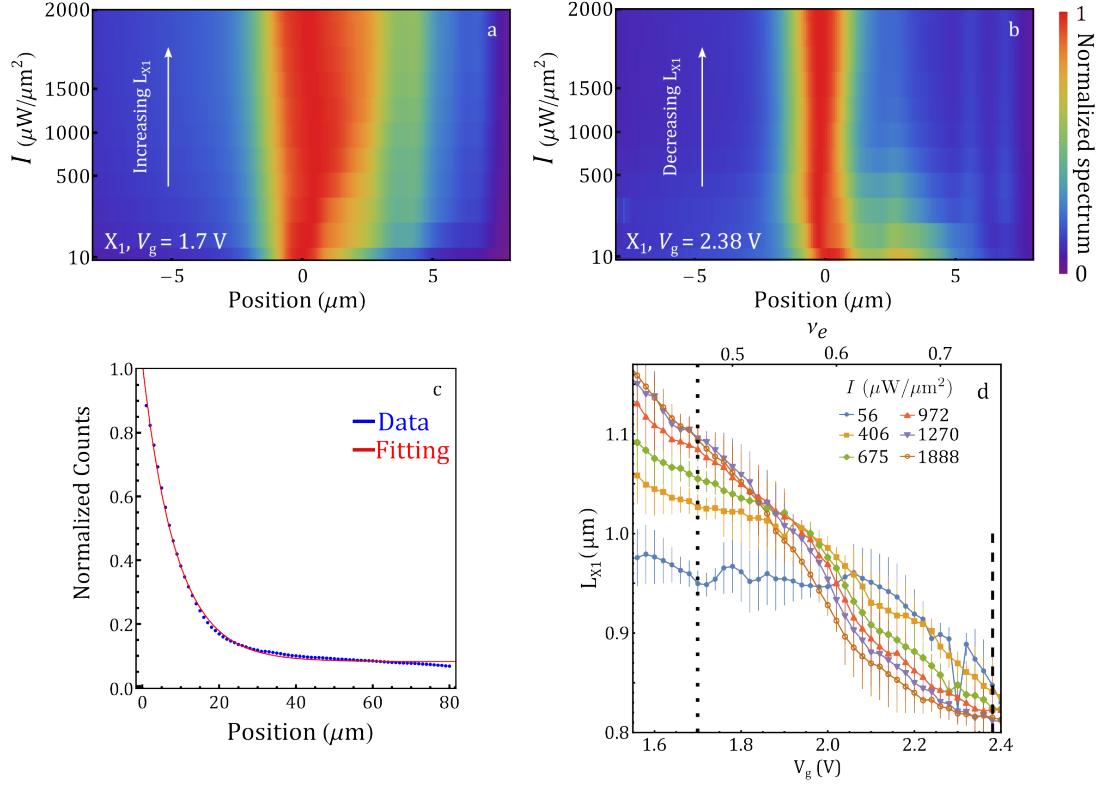
FIG. S6. (a-b) Pump intensity dependence of the X_1 spatial diffusion for $\nu_e \sim 0.47$ ($V_g = 1.7V$) (a) and $\nu_e \sim 0.75$ ($V_g = 2.38V$) (b). The panels show the inversion of the intensity dependence: from a diluted gas of bosons in panel a to a bosonic Mott insulator in panel b. (c) Exponential decay fitting of a typical X_1 diffusion pattern. (d) L_{X_1} for a reduced range of V_g to highlight the power dependence inversion.

image of the diffusion pattern is magnified 200 times. We spectrally resolve the signals emitted from X_1 and X_2. Next, we fit each spatial diffusion profile to a function of the form $A \exp\left(-x/L_{X_i}\right) + b$, where A is the PL power under the pumping laser spot, x is the propagation distance, L_{X_i} is the diffusion length of X_i and b is an offset that accounts for the base noise level. Fig. S6 (a-b) shows the obtained power dependence for L_{X_1} at $V_g = 1.7$ V and $V_g = 2.38$ V. We observe that L_{X_1} increases with pump power at 1.7 V but decreases at 2.38 V. This inversion in the power dependence accounts for the formation of incompressible excitonic states. It is worth mentioning that the scale of the I axis is not linear, because the power was modified by changing the polarization of the pump laser with a half-wave plate. Panel c shows the fitting subroutine used to extract the diffusion length of X_1. Panel d shows the measured value of L_{X_1} for a range of V_g to highlight the inversion of the intensity dependence. The same analysis was performed for the diffusion of the X_2 states. The data (Fig. S7a) shows a shorter diffusion length, which makes it cumbersome to detect changes in L_{X2} due to the diffraction limit. However, in contrast to L_{X1}, the L_{X2} increases with increasing V_g, except for the reduction at $\nu_e \sim 1$, which can be attributed to the behavior of a population of excitons in presence of a fermionic Mott insulating state. We finally analyze the diffusion data
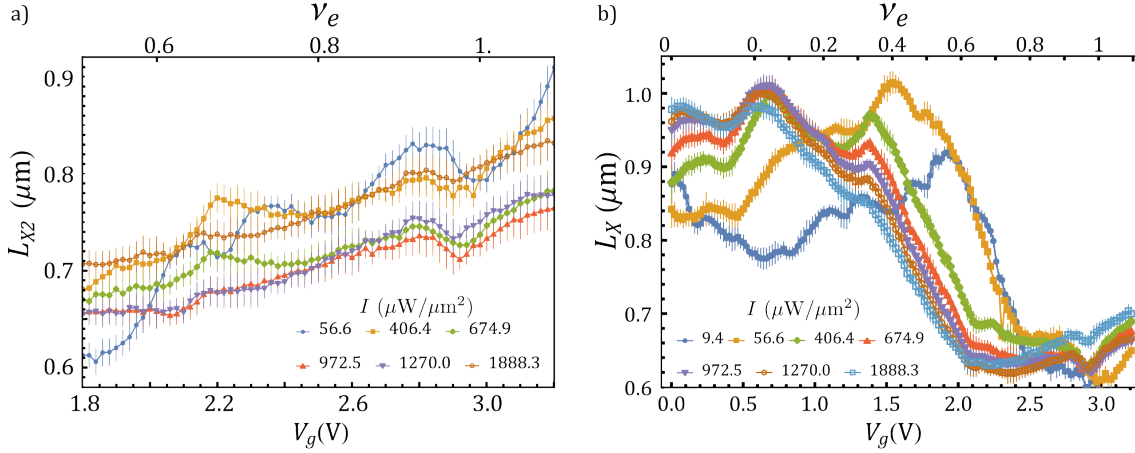
FIG. S7. (a)L_{X2} as a function of the gate voltage for a range of ν_e and for different I (b) L_X as a function of the gate voltage for a range of ν_e and for different I

with no spectral resolution. For $\nu_e < 1$, one can observe that the suppression of the diffusion takes place for lower V_g upon increasing pump intensity; a consequence of the bosonic saturation of the lattice due to the optical pump.

* These authors contributed equally to this work

† dsuarezf@umd.edu

‡ hafezi@umd.edu

[1] J. Hubbard, Electron correlations in narrow energy bands, Proceedings of the Royal Society of London. Series A. Mathematical and Physical Sciences **276**, 238 (1963).

[2] M. Greiner, O. Mandel, T. Esslinger, T. W. Hänsch, and I. Bloch, Quantum phase transition from a superfluid to a mott insulator in a gas of ultracold atoms, Nature 2002 415:6867 **415**, 39 (2002).

[3] I. Carusotto, A. A. Houck, A. J. Kollár, P. Roushan, D. I. Schuster, and J. Simon, Photonic materials in circuit quantum electrodynamics, Nature Physics 2020 16:3 **16**, 268 (2020).

[4] A. Ghiotto, E. M. Shih, G. S. Pereira, D. A. Rhodes, B. Kim, J. Zang, A. J. Millis, K. Watanabe, T. Taniguchi, J. C. Hone, L. Wang, C. R. Dean, and A. N. Pasupathy, Quantum criticality in twisted transition metal dichalcogenides, Nature 2021 597:7876 **597**, 345 (2021), arXiv:2103.09796.

[5] T. Li, S. Jiang, L. Li, Y. Zhang, K. Kang, J. Zhu, K. Watanabe, T. Taniguchi, D. Chowdhury, L. Fu, J. Shan, and K. F. Mak, Continuous Mott transition in semiconductor moiré superlattices, Nature 2021 597:7876 **597**, 350 (2021), arXiv:2103.09779.

[6] Y. Shimazaki, I. Schwartz, K. Watanabe, T. Taniguchi, M. Kroner, and A. Imamoğlu, Strongly correlated electrons and hybrid excitons in a moiré heterostructure, Nature 2020 580:7804 **580**, 472 (2020).

[7] Y. Tang, L. Li, T. Li, Y. Xu, S. Liu, K. Barmak, K. Watanabe, T. Taniguchi, A. H. MacDonald, J. Shan, and K. F. Mak, Simulation of Hubbard model physics in WSe2/WS2 moiré superlattices, Nature 2020 579:7799 **579**, 353 (2020).

[8] Y. Zhang, N. F. Q. Yuan, and L. Fu, Moiré quantum chemistry: Charge transfer in transition metal dichalcogenide superlattices, Physical Review B **102**, 201115 (2011).

[9] L. Wang, E. M. Shih, A. Ghiotto, L. Xian, D. A. Rhodes, C. Tan, M. Claassen, D. M. Kennes, Y. Bai, B. Kim, K. Watanabe, T. Taniguchi, X. Zhu, J. Hone, A. Rubio, A. N. Pasupathy, and C. R. Dean,

Correlated electronic phases in twisted bilayer transition metal dichalcogenides, Nature Materials 2020 19:8 **19**, 861 (2020).

[10] Y. Xu, S. Liu, D. A. Rhodes, K. Watanabe, T. Taniguchi, J. Hone, V. Elser, K. F. Mak, and J. Shan, Correlated insulating states at fractional fillings of moiré superlattices, Nature 2020 587:7833 **587**, 214 (2020).

[11] X. Huang, T. Wang, S. Miao, C. Wang, Z. Li, Z. Lian, T. Taniguchi, K. Watanabe, S. Okamoto, D. Xiao, S. F. Shi, and Y. T. Cui, Correlated insulating states at fractional fillings of the WS2/WSe2 moiré lattice, Nature Physics 2021 17:6 **17**, 715 (2021), arXiv:2007.11155.

[12] E. C. Regan, D. Wang, C. Jin, M. I. Bakti Utama, B. Gao, X. Wei, S. Zhao, W. Zhao, Z. Zhang, K. Yumigeta, M. Blei, J. D. Carlström, K. Watanabe, T. Taniguchi, S. Tongay, M. Crommie, A. Zettl, and F. Wang, Mott and generalized Wigner crystal states in WSe2/WS2 moiré superlattices, Nature 2020 579:7799 **579**, 359 (2020).

[13] H. Li, S. Li, E. C. Regan, D. Wang, W. Zhao, S. Kahn, K. Yumigeta, M. Blei, T. Taniguchi, K. Watanabe, S. Tongay, A. Zettl, M. F. Crommie, and F. Wang, Imaging two-dimensional generalized Wigner crystals, Nature 2021 597:7878 **597**, 650 (2021).

[14] W. Li, L. M. Devenica, J. Zhang, Y. Zhang, X. Lu, K. Watanabe, T. Taniguchi, A. Rubio, and A. Srivastava, Local sensing of correlated electrons in dual-moiré heterostructures using dipolar excitons, (2021), arXiv:2111.09440 [cond-mat.mes-hall].

[15] L. Zhang, F. Wu, S. Hou, Z. Zhang, Y. H. Chou, K. Watanabe, T. Taniguchi, S. R. Forrest, and H. Deng, Van der Waals heterostructure polaritons with moiré-induced nonlinearity, Nature 2021 591:7848 **591**, 61 (2021), arXiv:2111.00638.

[16] C. Jin, Z. Tao, T. Li, Y. Xu, Y. Tang, J. Zhu, S. Liu, K. Watanabe, T. Taniguchi, J. C. Hone, L. Fu, J. Shan, and K. F. Mak, Stripe phases in WSe2/WS2 moiré superlattices, Nature Materials 2021 20:7 **20**, 940 (2021), arXiv:2007.12068.

[17] X. Wang, C. Xiao, H. Park, J. Zhu, C. Wang, T. Taniguchi, K. Watanabe, J. Yan, D. Xiao, D. R. Gamelin, W. Yao, and X. Xu, Light-induced ferromagnetism in moiré superlattices, Nature 2022 604:7906 **604**, 468 (2022), arXiv:2203.07161.

[18] I. Carusotto and C. Ciuti, Quantum fluids of light, Reviews of Modern Physics **85**, 299 (2013).

[19] J. Bloch, A. Cavalleri, V. Galitski, M. Hafezi, and A. Rubio, Strongly correlated electron–photon systems, Nature 2022 606:7912 **606**, 41 (2022).

[20] K. Xu, Y. Xu, H. Zhang, B. Peng, H. Shao, G. Ni, J. Li, M. Yao, H. Lu, H. Zhu, and C. M. Soukoulis, The role of Anderson's rule in determining electronic, optical and transport properties of transition metal dichalcogenide heterostructures, Physical Chemistry Chemical Physics **20**, 30351 (2018).

[21] K. Günter, T. Stöferle, H. Moritz, M. Köhl, and T. Esslinger, Bose-fermi mixtures in a three-dimensional optical lattice, Physical Review Letters **96**, 180402 (2006).

[22] S. Miao, T. Wang, X. Huang, D. Chen, Z. Lian, C. Wang, M. Blei, T. Taniguchi, K. Watanabe, S. Tongay, Z. Wang, D. Xiao, Y. T. Cui, and S. F. Shi, Strong interaction between interlayer excitons and correlated electrons in WSe2/WS2 moiré superlattice, Nature Communications 2021 12:1 **12**, 1 (2021).

[23] Y. Bai, S. Liu, Y. Guo, J. Pack, J. Wang, C. R. Dean, J. Hone, and X. Y. Zhu, Evidence for exciton crystals in a 2d semiconductor heterotrilayer, (2022), arXiv:2207.09601 [cond-mat.mes-hall].

[24] R. Ma, B. Saxberg, C. Owens, N. Leung, Y. Lu, J. Simon, and D. I. Schuster, A dissipatively stabilized mott insulator of photons, Nature **566**, 51 (2019).

[25] Y. Jiang, S. Chen, W. Zheng, B. Zheng, and A. Pan, Interlayer exciton formation, relaxation, and transport in TMD van der Waals heterostructures, Light: Science & Applications 2021 10:1 **10**, 1 (2021).

[26] L. A. Jauregui, A. Y. Joe, K. Pistunova, D. S. Wild, A. A. High, Y. Zhou, G. Scuri, K. de Greve, A. Sushko, C. H. Yu, T. Taniguchi, K. Watanabe, D. J. Needleman, M. D. Lukin, H. Park, and P. Kim, Electrical control of interlayer exciton dynamics in atomically thin heterostructures, Science **366**, 870 (2019), arXiv:1812.08691.

[27] D. Unuchek, A. Ciarrocchi, A. Avsar, Z. Sun, K. Watanabe, T. Taniguchi, and A. Kis, Valley-polarized exciton currents in a van der Waals heterostructure, Nature Nanotechnology 2019 14:12 **14**, 1104 (2019).

[28] T. S. Huang, Y.-Z. Chou, C. L. Baldwin, F. Wu, and M. Hafezi, Mott-moiré excitons 10.48550/arxiv.2207.13152 (2022).

[29] Y. H. Zhang, Doping a Mott insulator with excitons in a moiré bilayer: Fractional superfluid, neutral Fermi surface, and Mott transition, Physical Review B **106**, 195120 (2022), arXiv:2204.10937.

[30] A. Szasz, J. Motruk, M. P. Zaletel, and J. E. Moore, Chiral spin liquid phase of the triangular lattice hubbard model: A density matrix renormalization group study, Phys. Rev. X **10**, 021042 (2020).

[31] W. Kadow, L. Vanderstraeten, and M. Knap, Hole spectral function of a chiral spin liquid in the triangular lattice hubbard model, Phys. Rev. B **106**, 094417 (2022).

[32] L. Rademaker, Spin-orbit coupling in transition metal dichalcogenide heterobilayer flat bands, Phys. Rev. B **105**, 195428 (2022).

[33] D. Kiese, Y. He, C. Hickey, A. Rubio, and D. M. Kennes, Tmds as a platform for spin liquid physics: A strong coupling study of twisted bilayer wse2, APL Materials **10**, 031113 (2022).

[34] H. Li, U. Kumar, K. Sun, and S.-Z. Lin, Spontaneous fractional chern insulators in transition metal dichalcogenide moiré superlattices, Phys. Rev. Res. **3**, L032070 (2021).

[35] V. Crépel and L. Fu, Anomalous hall metal and fractional chern insulator in twisted transition metal dichalcogenides, (2022), arXiv:2207.08895 [cond-mat.str-el].

[36] R. Xiong, J. H. Nie, S. L. Brantly, P. Hays, R. Sailus, K. Watanabe, T. Taniguchi, S. Tongay, and C. Jin, Bosonic mott insulator in wse2/ws2 moiré superlattice, (2022).

[37] P. J. Zomer, M. H. D. Guimarães, J. C. Brant, N. Tombros, and B. J. van Wees, Fast pick up technique for high quality heterostructures of bilayer graphene and hexagonal boron nitride, Applied Physics Letters **105**, 013101 (2014).

[38] H. C. P. Movva, B. Fallahazad, K. Kim, S. Larentis, T. Taniguchi, K. Watanabe, S. K. Banerjee, and E. Tutuc, Density-dependent quantum hall states and zeeman splitting in monolayer and bilayer wse$_2$, Phys. Rev. Lett. **118**, 247701 (2017).